Wind Energ. Sci. Discuss., doi:10.5194/wes-2016-6, 2016
Manuscript under review for journal Wind Energ. Sci.
Published: 11 May 2016
© Author(s) 2016. CC-BY 3.0 License.



eawe european academy of wind energy
Open Access WIND ENERGY SCIENCE DISCUSSIONS

Multi-fidelity Fluid-Structure Interaction Analysis of a Membrane Blade Concept in non-rotating, uniform flow condition

Mehran Saeedi, Kai-Uwe Bletzinger, and Roland Wüchner
Lehrstuhl für Statik, Technical University of Munich, 80333 Munich, Germany
Correspondence to: M. Saeedi (mehran.saeedi@tum.de)

Abstract. In order to study the aerodynamic performance of a semi-flexible membrane blade, Fluid-Structure Interaction simulations have been performed for a non-rotating blade under steady inflow condition. The studied concept blade has a length of about 5 meters. It consists of a rigid mast at the leading edge, ribs along the blade, tensioned edge cables at the trailing edge and membranes forming upper and lower surface of the blade. Equilibrium shape of membrane structures in absence of external loading depends on the location of the supports and the pre-stresses in the membranes and the supporting edge cables. Form finding analysis is used to find the equilibrium shape. The exact form of a membrane structure at the service condition depends on the internal forces and also on the external loads which in turn depend on the actual shape. As a result, two-way coupled Fluid-Structure Interaction (FSI) analysis is necessary to study this class of structures. The fluid problem has been modeled using two different approaches which are the vortex panel method and the numerical solution of the Navier-Stokes equations. Nonlinear analysis of the structural problem is performed using the Finite Element Method. The goal of the current study is twofold: First, to make a comparison between the converged FSI results obtained from the two different methods to solve the fluid problem. This investigation is a prerequisite for the development of an efficient and accurate multi-fidelity simulation concept for different design stages of the flexible blade. The second goal is to study the aerodynamic performance of the membrane blade in terms of lift and drag coefficient as well as lift to drag ratio and to compare them with those of the equivalent conventional rigid blade. The blade configuration from the NASA-Ames Phase VI rotor is taken as the baseline rigid blade configuration. The studied membrane blade shows a higher lift curve slope and higher lift to drag ratio compared with the rigid blade.

1 Introduction

Flexible wings have been the topic of many research programs. Different techniques have been used in order to bring flexibility to conventional wing configurations. They range from using new structural concepts for wing frame like telescopic spars Blondeau (2003) or morphing wing Bowmann (2007) to using smart materials in manufacturing of the wing Barbarino (2010). Whereas in active control concepts (like morphing wing), deformability is brought to the wing by the use of actuators, in passive control the wing is to some extend flexible and is deformed solely as a consequence of applied aerodynamic loads. In the case of passive control the final form of the wing is a result of the equilibrium between aerodynamic forces and internal structural forces and therefore it is not trivial to reach the desired final shape. With the increase in wind turbine's rotor diameter,

Wind Energ. Sci. Discuss., doi:10.5194/wes-2016-6, 2016
Manuscript under review for journal Wind Energ. Sci.
Published: 11 May 2016
© Author(s) 2016. CC-BY 3.0 License.



eawe european academy of wind energy
Open Access WIND ENERGY SCIENCE DISCUSSIONS

aeroelastic simulation of rotor blades to study their unsteady response to disturbances or control actions has become more and more important. To realize the so-called "smart rotors" both active Barlas (2016) and passive Bottasso (2016) aeroelastic devices have been studied for load mitigation of wind turbines.

Membrane wings have proved to be a good alternative to rigid wing constructions for Micro Air Vehicles (maximum dimension of $15cm$ by definition) Lian (2005), Abdulrahim (2005). The flexibility of a membrane wing enables it to adapt itself to the flow field to a certain extend. The advantages of this passive adaption to the surrounding flow are from aerodynamics point of view a higher lift slope, higher maximum lift coefficient and postponed stall to higher angles of attack compared to rigid wings Valasek (2012) and from the structural perspective, load reduction in unsteady flow cases Levin (2001). One drawback of flexible wings could be that because of their flexibility and due to self excited vibrations they could show unsteady response even to steady flow conditions Waszak (2001).

Specific Sailwing research was originally initiated at Princeton University during the 1970s with the interest in determining the applicability of this design as an auxiliary lifting device. Various studies were employed to explore the structural and aerodynamic characteristics of the sailwing. It was concluded that sailwings have favorable characteristics compared with conventional rigid wings. From the aerodynamics point of view, sailwings have a higher lift curve slope, a higher maximum lift coefficient and higher lift to drag ratio compared to an equivalent rigid wing Fink (1967); Maughmer (1979); Fink (1969); Saeedi (2015). Delayed stall to higher angles of attack is another advantage of membrane wings Maughmer (1979). From the structural dynamics point of view, there is a load reduction for membrane wings in unsteady flow cases Levin (2001). Later, during the 1980s, application of the sailwing concept in wind energy systems was explored by the Princeton windmill group. The final progress report of the group states Maughmer (1976): "the sailwing rotor continues to be highly competitive in performance with its rigid-bladed counterparts and yet enjoys the benefits of simpler construction and lower costs". The goal of the current contribution is to make a comparison between a membrane blade and its conventional rigid blade counterpart. The NASA-Ames Phase VI rotor Hand (2001) is chosen as the reference rigid blade configuration. The membrane blade uses the same planform as the NASA-Ames Phase VI rotor blade. Along the span, the blade is divided into 4 segments of equal span. The upper and lower surface of each segment is a pre-stressed membrane. The membranes are both connected to a pre-stressed cable at the trailing edge.

A membrane blade concept is studied in the current work which is mostly a passively controlled wing. Membrane structures are able to efficiently carry external loads over large spans via internal in-plane stresses. This optimal load carrying behavior is inherently accompanied by a significant flexibility. The structural response of such a wing to aerodynamic loads depends on the membrane's stresses, so two-way coupled fluid-structure interaction simulations (FSI) are necessary to analyze its behavior in operation. Numerous aeroelastic simulations might be needed to find the best set of pre-stresses and material parameters to ensure a better aerodynamic performance. This highlights the need for less complex (and thus computationally less expensive) fluid models for FSI simulations during early design stages. An alternative to the numerical simulation of the flow field using Navier-Stokes equations (NSE) is the vortex panel method. The panel method is computationally less demanding and enables a faster exploration of the design space. However, in general, it neglects viscous effects and therefore its range of applicability should be evaluated. In the current paper FSI simulations for the membrane blade concept have been performed using these

Wind Energ. Sci. Discuss., doi:10.5194/wes-2016-6, 2016
Manuscript under review for journal Wind Energ. Sci.
Published: 11 May 2016
© Author(s) 2016. CC-BY 3.0 License.



eawe european academy of wind energy
Open Access WIND ENERGY SCIENCE DISCUSSIONS

two approaches for the fluid side and the results are systematically compared. Aerodynamic performance of the membrane blade is checked against its equivalent rigid blade as well.

Analysis of the membrane blade consists of three major steps. They are represented in Figure 1 for a sample section. In the form finding step, the equilibrium shape in absence of external loading is calculated, which is the shape at the beginning of FSI simulation. Then in FSI analysis, the interaction between the membrane and the fluid flow is simulated. The FSI analysis is followed by evaluation of the design in terms of aerodynamic and structural characteristics of the blade. The cycle could be repeated for a new design to realize a better performance of the blade.

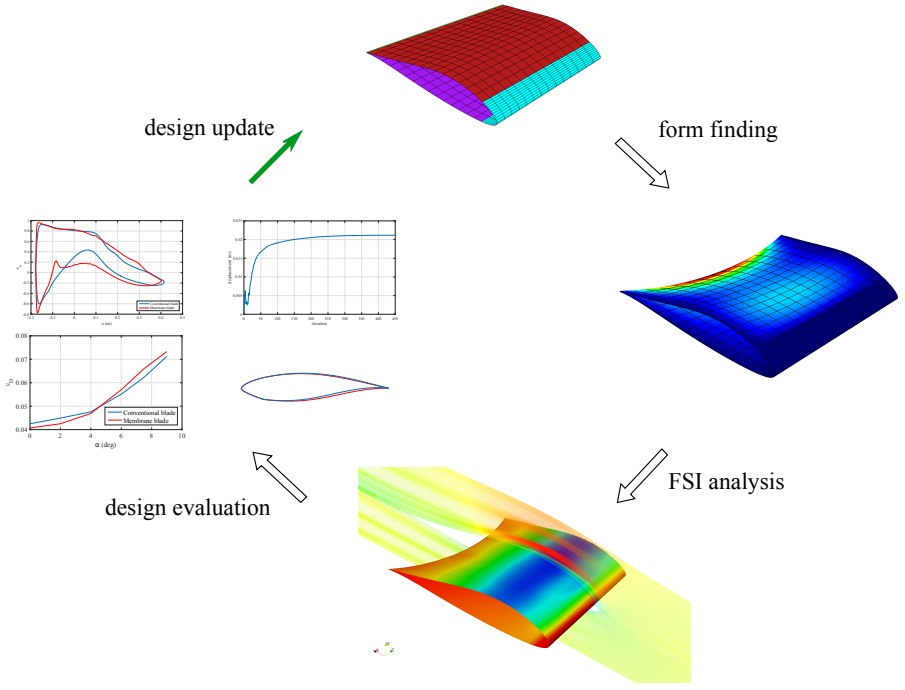

Figure 1. Anylsis workflow for the membrane blade

This paper has the following structure. Section 2 describes the membrane blade concept and the procedure of its design and analysis, followed by the theory of fluid and structure part as well as the coupling concept used in FSI simulations. Next, in section 3, the model set-up for the simulations and the results are presented. The paper closes by section 4, where the conclusions are summarized.

Wind Energ. Sci. Discuss., doi:10.5194/wes-2016-6, 2016
Manuscript under review for journal Wind Energ. Sci.
Published: 11 May 2016
© Author(s) 2016. CC-BY 3.0 License.



eawe european academy of wind energy
Open Access WIND ENERGY SCIENCE DISCUSSIONS

2 Membrane Blade Concept and FSI Simulation Strategy

Fig. 2 shows the membrane wing concept studied in the current work. A rigid mast forms the leading edge section of the wing. To support the upper and lower membranes, ribs are mounted along the span of the wing and their number depends on the span length of the wing. Upper and lower membranes are joined together at the trailing edge via a pre-tensioned edge cable.

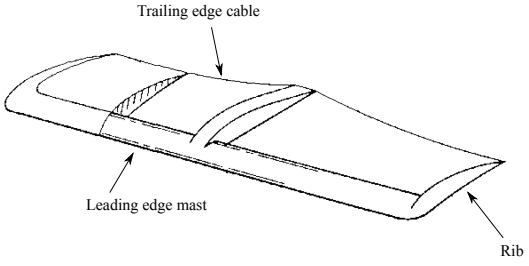

Figure 2. Sailwing construction concept, from Ormiston (1971)

In case of a flexible membrane blade, the shape of the blade's surface depends on the one hand on the working conditions in terms of wind speed, angle of attack, etc. and on the other hand on the structural properties of its supporting frame and the membranes which form the wing surface. The pressure distribution on the surface of the wing depends on the form and the above mentioned working condition. Structural properties of the wing govern its deformation under such a loading. The final form of the wing results from this interaction between loading and displacement. This emphasizes the necessity of FSI simulations for the analysis of such a wing concept. FSI simulations are computationally complex and time-consuming. From the fluid point of view, turbulent flow should be simulated using either LES or RANS turbulence models and on the structural side nonlinear dynamic or static analysis is needed in order to correctly deal with large displacements which occur in the membranes. The analysis starts with form finding simulation. In form finding, the equilibrium state of the wing is calculated, i.e. the state where membrane and edge cable internal forces are in equilibrium is computed. This is the initial shape of the blade surface in the absence of external forces. FSI simulations are started from this initial state. In the following sections, fluid, structure and coupling related aspects are explained in detail. The overall simulation work flow is shown in Fig 3, which demonstrates the sequence of the simulations.

The process of solving the flow problem for both approaches is presented in the figure as well. At each coupling iteration the fluid solver receives the displacement from the structural solver and updates the mesh. Then the fluid problem is solved for the updated mesh. It should be noted that in solving the problem using finite volume method all the steps include operations performed on a three dimensional mesh, while in panel method the mesh consists of two dimensional surface discretization. For the case of mesh update in particular, for the panel method discretization updating the mesh means adding the displacement at each node to the original coordinate of the node, but for the three-dimensional volume mesh, in addition to applying the displacement on the boundary the displacement of the interior points should also be calculated. In addition to the higher

Wind Energ. Sci. Discuss., doi:10.5194/wes-2016-6, 2016
Manuscript under review for journal Wind Energ. Sci.
Published: 11 May 2016
© Author(s) 2016. CC-BY 3.0 License.



computational cost of the three-dimensional mesh morphing, it is also a challenge to keep the the quality of the volume elements as they deform.

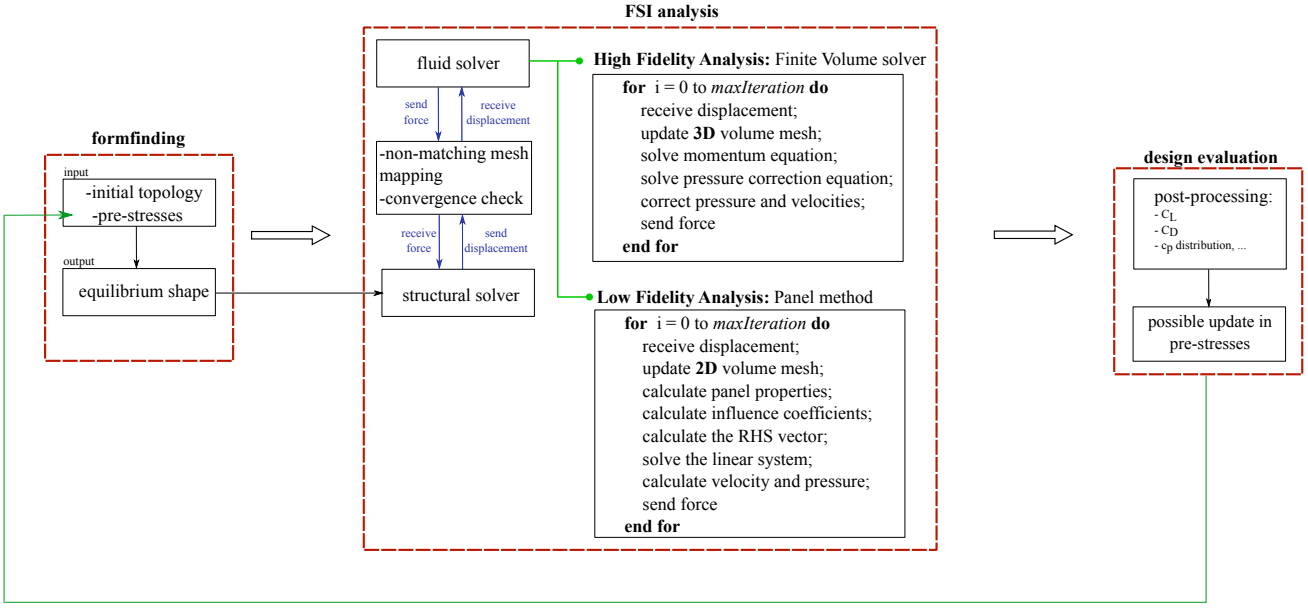

Figure 3. Schematic representation of the multi-fidelity analysis work flow

2.1 Fluid Model

Two approaches of very different fidelity are used for the modeling and simulation of fluid flow. The first one is the finite volume based numerical solution of Navier-Stokes equations using OpenFOAM and the second one is the vortex panel method. The advantage of the vortex panel method is that it is computationally less demanding, while its drawback is that it neglects the viscous effects. Still it is a very good alternative to Navier-Stokes during the early design stages. While a steady state FSI simulation using the first approach takes about 10 hours to converge, the same simulation takes about 20 minutes to converge to the steady-state solution using vortex panel method. Even though some details of fluid flow are neglected in vortex panel method, the fact that it is much faster than solving Navier-Stokes equations enables design space explorations at reasonable computational costs in a certain range of operating conditions

Wind Energ. Sci. Discuss., doi:10.5194/wes-2016-6, 2016
Manuscript under review for journal Wind Energ. Sci.
Published: 11 May 2016
© Author(s) 2016. CC-BY 3.0 License.



2.1.1 Navier-Stokes Equations

The NS equations are the general equations describing the flow of fluid substances. For incompressible fluid flow with constant viscosity they read:

$$\nabla \cdot (\rho \mathbf{v}) = 0 \tag{1}$$

and

$$\rho(\frac{\partial \mathbf{v}}{\partial t} + \mathbf{v}.\nabla \mathbf{v}) = -\nabla p + \mu \nabla^2 \mathbf{v} + \mathbf{f}. \tag{2}$$

Velocity ($\mathbf{v}$) and pressure (p) fields are coupled in these equations. SIMPLE algorithm of Patankar and Spalding Patankar (1972) is used to enforce the coupling. Reynolds averaged Navier-Stokes model is used for turbulence modeling and turbulent viscosity is modeled using $k-\omega SST$ model Menter (1994). It is a two equation model used to calculate kinematic eddy viscosity. First the equations for turbulent kinetic energy (k) and specific dissipation rate (ω) are solved. Kinematic eddy viscosity is then calculated from k, ω and other parameters of the model.

Appart from solving the fluid flow problem, in a FSI simulation the fluid solver should take care of the displacement in FSI interface and needs to update the mesh at each iteration, since the fluid domain changes after each iteration. As a result, the mesh needs to be updated correspondingly. One solution could be re-meshing of the updated domain at each iteration, which is computationally very expensive. The other way to deal with the problem is to apply the displacement at the FSI interface to the original mesh and update it by solving the mesh motion problem. The boundary conditions for the mesh motion problem are the prescribed displacements at the boundaries of the domain and at the FSI interface. The problem is then solved for calculating the displacement of the internal points.

2.1.2 Vortex Panel Method

The velocity field for the case of irrotational, incompressible and inviscid flow can be represented by a velocity potential Φ. This is the basis for vortex panel method. The flow velocity can be calculated from the potential in the following way:

$$u = -\frac{\partial \Phi}{\partial x}, \tag{3}$$

$$v = -\frac{\partial \Phi}{\partial y}, \tag{4}$$

$$w = -\frac{\partial \Phi}{\partial z}. \tag{5}$$

Inserting the above equations into continuity equation (1) results in the continuity equation in terms of the potential:

$$\nabla^2 \Phi = 0. \tag{6}$$

Wind Energ. Sci. Discuss., doi:10.5194/wes-2016-6, 2016
Manuscript under review for journal Wind Energ. Sci.
Published: 11 May 2016
© Author(s) 2016. CC-BY 3.0 License.



eawe european academy of wind energy
Open Access WIND ENERGY SCIENCE DISCUSSIONS

This equation can be solved by superposition of elementary solutions. There are two boundary conditions for solving this Laplacian equation. One is that for a body submerged in fluid the velocity component normal to body's surface should vanish:

$$\nabla\Phi \cdot \mathbf{n} = 0, \tag{7}$$

where $\mathbf{n}$ is the vector normal to the surface. The other condition is that the disturbance in the free stream flow caused by the elementary solutions should vanish as the distance, r, from the boundary surface increases:

$$\lim_{\mathbf{r}\to\infty} \nabla\Phi = 0. \tag{8}$$

Using the Green's identity it can be shown that the potential at each point, P, inside the domain can be calculated in terms of the potential (Φ) and its derivative ($\frac{\partial\Phi}{\partial\mathbf{n}}$) on the boundary of the domain:

$$\Phi(P) = \frac{1}{4\pi}\int_S (\frac{1}{r}\nabla\Phi - \Phi\nabla\frac{1}{r}) \cdot \mathbf{n} dS \tag{9}$$

Detailed derivation of (9) is available in Katz (2008). The problem is now reduced to finding the values of the potential on the boundary which fulfill the continuity equation (6) and the two boundary conditions stated in (7) and (8). Laplace equation is a linear equation and if two functions fulfill the equation, their linear combination fulfills the equation as well. Hence, the solution of the continuity equation can be found as a superposition of elementary solutions like sources and doublets on the boundary of the domain. For a point source with strength of σ we have:

$$\Phi = -\frac{\sigma}{4\pi r} \tag{10}$$

and

$$\mathbf{v}(P) = \frac{\sigma}{4\pi}\frac{\mathbf{r}}{r^3} \tag{11}$$

where $\mathbf{r}$ is the vector from the point source to the point P and r is its magnitude. For a point doublet with strength of μ the potential reads:

$$\Phi = \frac{\mu}{4\pi}\mathbf{n} \cdot \nabla(\frac{1}{r}) \tag{12}$$

and the three components of the velocity vector ($\mathbf{V} = (u, v, w)$), at a point $P = (x, y, z)$ due to a point doublet located at (x_0, y_0, z_0) are

$$u = -\frac{\mu}{4\pi}\frac{(y-y_0)^2 + (z-z_0)^2 - 2(x-x_0)^2}{[(x-x_0)^2 + (y-y_0)^2 + (z-z_0)^2]^{\frac{5}{2}}}, \tag{13}$$

$$v = \frac{3\mu}{4\pi}\frac{(x-x_0)(y-y_0)}{[(x-x_0)^2 + (y-y_0)^2 + (z-z_0)^2]^{\frac{5}{2}}}, \tag{14}$$

and

$$w = \frac{3\mu}{4\pi}\frac{(x-x_0)(z-z_0)}{[(x-x_0)^2 + (y-y_0)^2 + (z-z_0)^2]^{\frac{5}{2}}}. \tag{15}$$

Wind Energ. Sci. Discuss., doi:10.5194/wes-2016-6, 2016
Manuscript under review for journal Wind Energ. Sci.
Published: 11 May 2016
© Author(s) 2016. CC-BY 3.0 License.



eawe european academy of wind energy
Open Access WIND ENERGY SCIENCE DISCUSSIONS

The elementary solutions automatically satisfy the constraint that they should decay as the distance increases. Their resulting velocity vanishes as r tends to infinity. But the velocity goes to infinity as r tends to 0. That is why they are called singular solutions. In panel method the strength of these singular solutions are calculated using the boundary condition stated in (7) to enforce zero normal velocity at the surface of the boundary. The surface of the wing is discretized with a number of panels as shown in Fig. 4. Each panel on the wing surface represents a quadrilateral source and a quadrilateral doublet element. In addition to wing panels there are wake panels to represent the wake behind the wing. Wake panels consist of quadrilateral doublets.

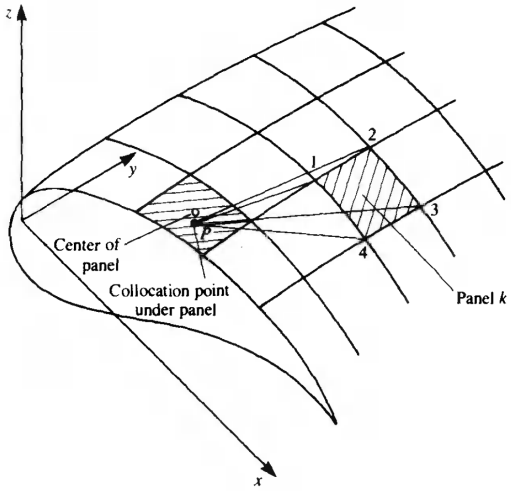

Figure 4. Discretization of the wing surface into panels, from Katz (2008)

There are two ways to enforce the zero normal flow boundary condition. It can be enforced as a Dirichlet boundary condition by setting a constant value for the potential inside the body or as a Neumann boundary condition which deals with the derivative of the potential, i.e. the velocity. We have used the latter implementation of this boundary condition for the collocation point at each panel. The collocation point of a panel is at the center of the panel (in the case of Dirichlet boundary condition the collocation points are infinitesimally shifted inside the body). The velocity at collocation point P is calculated by summing up the contribution of each panel to the velocity at this point:

$$\mathbf{v}(P) = \sum_{k=1}^{N} \mathbf{C}_k \mu_k + \sum_{l=1}^{N_w} \mathbf{C}_l \mu_l + \sum_{k=1}^{N} \mathbf{B}_k \sigma_k, \tag{16}$$

where N is the number of panels on the wing's surface and N_w is the number of wake panels. The first term in (16) is for the contribution of doublet elements on the wing panel, the second represents the contribution of doublet element at the wake and finally the last one is for source terms on the wing. $\mathbf{C}_k$ can be interpreted as the velocity caused by the kth panel at point P, it is calculated for a panel of unit strength. The same interpretation holds for $\mathbf{B}_k$ regarding the source terms. For more details on the calculation of the influence coefficients $\mathbf{C}_k$ and $\mathbf{B}_k$ we refer the reader to Katz (2008). The total velocity at the point P is

Wind Energ. Sci. Discuss., doi:10.5194/wes-2016-6, 2016
Manuscript under review for journal Wind Energ. Sci.
Published: 11 May 2016
© Author(s) 2016. CC-BY 3.0 License.



eawe european academy of wind energy
Open Access WIND ENERGY SCIENCE DISCUSSIONS

the velocity caused by the panels plus the free stream velocity. To set the total velocity in the normal direction to the panel to zero, the contribution of panels should cancel out that of the free stream velocity:

$$\left(\sum_{k=1}^{N}\mathbf{C}_k\mu_k+\sum_{l=1}^{N_w}\mathbf{C}_l\mu_l+\sum_{k=1}^{N}\mathbf{B}_k\sigma_k\right)\cdot\mathbf{n}=-\mathbf{v}_\infty\cdot\mathbf{n}. \tag{17}$$

Equation (17) should hold at every collocation point. Applying this equation to each collocation point we end up with a system of N equations with N unknowns. This system of linear equations is then solved for the unknowns which are the strengths of the doublet panels. It should be mentioned that the strength of the k^{th}source panels is already set to

$$\sigma(k)=\mathbf{v}_\infty\cdot\mathbf{n}(k) \tag{18}$$

and is moved to the right hand side before solving the system of linear equations. $\mathbf{v}_\infty$ is the free stream velocity vector. The strength of wake panels is also calculated in terms of doublet strength at the upper and lower neighboring panels of the trailing edge (Fig. 5) using the Kutta condition.

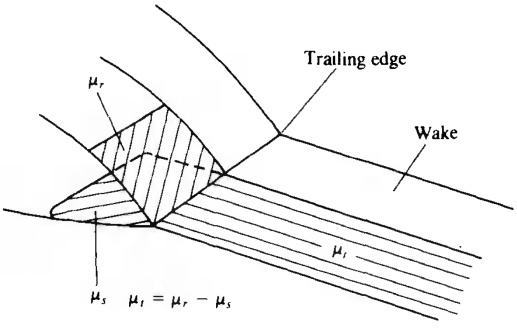

Figure 5. Wake panels used to apply the Kutta condition, from Katz (2008)

The Kutta condition implies that the circulation at the trailing edge should be zero. Three panels intersect at the trailing edge. These are the wake panel and the two wing panels on the upper and lower surface of the wing. The Kutta condition is satisfied by setting the difference in the strength of upper and lower panel to wake strength:

$$\mu_w=\mu_{upper}-\mu_{lower}. \tag{19}$$

Strength of the doublet panels are calculated by solving the resulting system of linear equations. In the post-processing step the velocity at the points of interest, which are the collocation points in particular, is calculated. The pressure is then calculated from the steady state Bernoulli equation. Using the Bernoulli equation, the pressure coefficient reads:

$$c_p=\frac{p-p_\infty}{\frac{1}{2}\rho V_\infty^2}=1-\left(\frac{\|\mathbf{v}\|}{\|\mathbf{v}_\infty\|}\right)^2. \tag{20}$$

Fig. 6 shows the calculated pressure distribution at the middle section of a NACA0012 wing for an angle of attack of 6 degrees. The results are compared with the ones from XFLR5 to check the correctness of developed panel solver which is used in the remainder of this publication as a low-fidelity fluid solver.

Wind Energ. Sci. Discuss., doi:10.5194/wes-2016-6, 2016
Manuscript under review for journal Wind Energ. Sci.
Published: 11 May 2016
© Author(s) 2016. CC-BY 3.0 License.



eawe european academy of wind energy
Open Access WIND ENERGY SCIENCE DISCUSSIONS

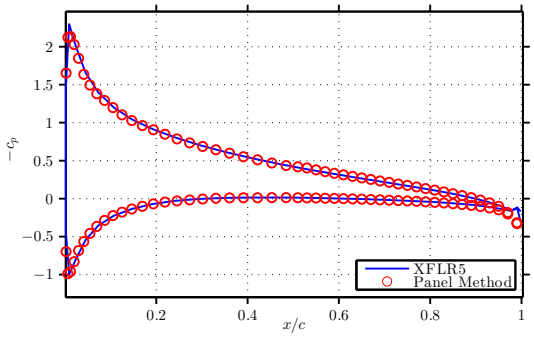

Figure 6. Pressure distribution over a NACA0012 wing section, $\alpha = 6^\circ$

2.2 Structural Model

The simulation of membrane structures typically consists of two steps: form finding and nonlinear static or dynamic analysis. In general structural analysis of membranes using the finite element method is used and displacements are calculated for a specific structure under applied load. Form Finding of membrane structures can be seen as the inverse problem of structural analysis. Pre-stressed membrane structures can be supported at the edges by pre-tensioned edge cables. In the inverse problem of form finding the stresses in membrane and edge cables are given and support conditions (fixed boundaries) are defined. The goal of the form finding analysis is to find the shape at which an equilibrium between structural forces exists. In other words, form finding analysis calculates the equilibrium shape of the membrane enclosed by a given boundary and with predefined stress distributions. It has been inspired e.g. by the works of the German architect, Frei Otto Otto (1995), and was originally developed for form finding of cable structures. Form finding could be done using different approaches like Force Density Method Schek (1974), Dynamic Relaxation Wakefield (1999) or Updated Reference Strategy (URS) Bletzinger (1997), Wüchner (2005). We have used the URS based method available in the in-house structural solver CARAT++. As a classical form finding example, the 4 point tent is presented in Figure 7. The reference configuration of the 4 point tent example consists of four flat membrane patches. They are connected to four edge cables at the boundaries and are fixed at four support points. After applying pre-stresses to the 4 membranes and the supporting edge cables, the structure evolves from flat membranes to a double curved surface where internal membrane pre-stresses are in equilibrium with the forces from the 4 edge cables.

CARAT++ has also been used for performing static nonlinear FEM analysis using the load-control method. This starts from the equilibrium state and computes the deformations due to the external loads caused by the fluid flow.

2.3 Fluid-Structure Interaction

Fluid-Structure Interaction studies the interaction between a solid body and its surrounding fluid. The interface between the fluid field (Ω_F) and the structure field (Ω_S) is designated by Γ_I. The load from the fluid field is coupled with the displacement from the structure field. There are two coupling conditions enforced at the interface:

Wind Energ. Sci. Discuss., doi:10.5194/wes-2016-6, 2016
Manuscript under review for journal Wind Energ. Sci.
Published: 11 May 2016
© Author(s) 2016. CC-BY 3.0 License.



eawe european academy of wind energy
Open Access WIND ENERGY SCIENCE DISCUSSIONS

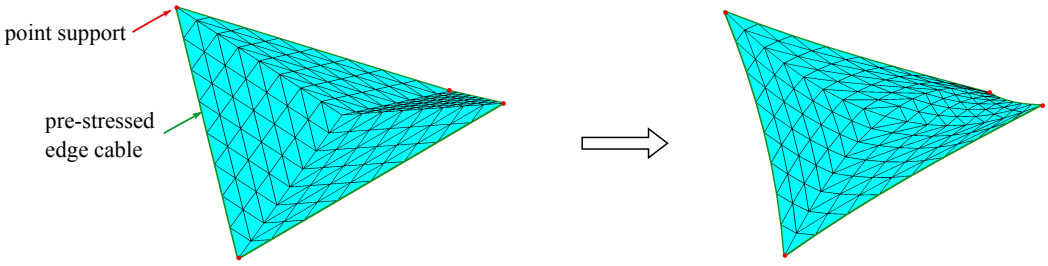

Figure 7. Form finding analysis of a 4 point tent. Left: initial state. Right: equilibrium state

Kinematic continuity condition

Enforcing this constraint ensures that the fluid and structure interfaces lie on each other during the simulation. It is satisfied if the displacement at the fluid interface is the same as the displacement at the solid interface:

$$\mathbf{d}^F_{\Gamma_I}(t) = \mathbf{d}^S_{\Gamma_I}(t). \tag{21}$$

Dynamic continuity condition

Dynamic continuity condition is about mapping the correct force vector from the fluid interface to the solid interface. It implies:

$$\mathbf{f}^S_{\Gamma_I}(t) = \mathbf{f}^F_{\Gamma_I}(t). \tag{22}$$

The interface mesh at the fluid side is in most cases finer than the mesh at the structure side. Non-matching mapping techniques Wang (2016) are necessary to map the equivalent nodal force and nodal displacement at the FSI interface. There are two classes of methods for tackling a FSI problem: Monolithic and partitioned solution schemes. In the monolithic approach, fluid and structure equations are merged into a single system of equations and are solved simultaneously, while in the partitioned approach the problem is divided into two separate sub-problems for fluid and structure field Wüchner (2007) . Each field is solved separately in the partitioned approach and exchange of information takes place in a separate coupling step. Monolithic approach has typically an advantage over the partitioned one in terms of stability and accuracy Kupzok (2009). On the other hand, solving the two fields independently in a modular environment, provides the possibility of using the most efficient available solution techniques for each field. Thus, this is the preferred simulation approach to develop the multi-fidelity analysis concept.

For steady state FSI simulation the coupling steps in each iteration are as follows:

1. Solve the fluid problem for the new iteration $(n+1)$
2. Send the resulting force at the interface to the structure solver
3. Solve the structure problem

Wind Energ. Sci. Discuss., doi:10.5194/wes-2016-6, 2016
Manuscript under review for journal Wind Energ. Sci.
Published: 11 May 2016
© Author(s) 2016. CC-BY 3.0 License.



eawe european academy of wind energy
Open Access WIND ENERGY SCIENCE DISCUSSIONS

4. Send the calculated displacement to the fluid solver and proceed to the next iteration

Schematic representation of these steps is shown in figure 8.

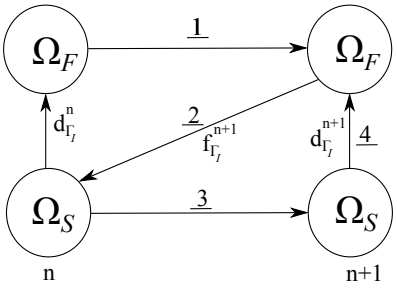

Figure 8. Solution procedure for the coupled problem

In the following the structure problem is abbreviated by the operator S and the fluid problem by the operator F. On the structure side the solver receives the loading from the fluid solvers and calculates the displacement at the interface:

$$\mathbf{d}_{\Gamma_I}^{n+1} = S(\mathbf{f}_{\Gamma_I}^{n+1}) \tag{23}$$

For the fluid solver it is just the opposite, it receives the displacement at the interface and delivers the load applied by the fluid:

$$\mathbf{f}_{\Gamma_I}^{n+1} = F(\mathbf{d}_{\Gamma_I}^{n}) \tag{24}$$

Inserting $\mathbf{d}_\Gamma$ from equation 23 into equation 24 we have:

$$\mathbf{d}_{\Gamma_I}^{n+1} = S(\mathbf{f}_{\Gamma_I}^{n+1}) = S\Big(F(\mathbf{d}_{\Gamma_I}^{n+1})\Big) = S \circ F(\mathbf{d}_{\Gamma_I}^{n}) \tag{25}$$

Equation 25 could be solved either using fixed-point iteration based methods or Newton-based methods. In the current work Gauss-Seidel method is used to solve the equation iteratively. The convergence of the iterative solution procedure is checked during the iteration steps by comparing the current solution with the previous solution. A relative tolerance of 10^{-6} is used as the convergence criterion.

3 Results

The studied membrane blade can be seen in Fig. 9. It is inspired by the layout of the rigid NASA-Ames Phase VI rotor with a length of 5.029 m Hand (2001). The chord length varies along the blade, with $0.73m$ at the root of the blade (after the transition from cylindrical hub profile to the airfoil profile) to $0.35m$ at the tip of the blade. Upper and lower membranes are wrapped around the rigid leading edge which extends up to 15% of the chord length. The membranes are supported by 4 ribs and by an edge cable at the trailing edge. The 4 ribs divide the blade into 4 segments with equal span. Structural properties of the membranes, ribs (which are modeled as beams) and edge cable are summarized in Tables 1 to 3. The pre-stresses in table 1 are for the first blade section from the root. The pre-stress in span direction is the same for all 4 segments, since they all have the same span, but the pre-stress in chord direction is scaled with the mean chord length for the three other segments.

Wind Energ. Sci. Discuss., doi:10.5194/wes-2016-6, 2016
Manuscript under review for journal Wind Energ. Sci.
Published: 11 May 2016
© Author(s) 2016. CC-BY 3.0 License.



eawe european academy of wind energy
Open Access WIND ENERGY SCIENCE DISCUSSIONS

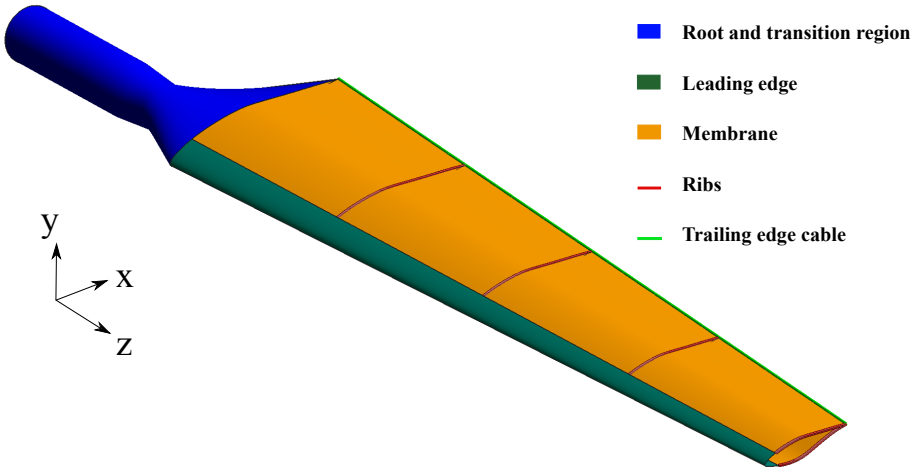

Figure 9. Blade planform

3.1 Form Finding

The equilibrium state of the blade with structural parameters presented in the Tables 1 to 3 is calculated in a form finding analysis. The deformed state is compared with the undeformed state in Fig. 10. Membranes and the edge cables pull against each other and as a result, the edge cables are moved toward the leading edge with maximum displacement at the middle of each blade segment. The pre-stresses in the membranes form double-curved membrane surfaces, where the upper membranes are moved downwards and lower membranes are moved upwards. While the cross section remains unchanged at the 4 ribs, due to the deformation of the two membranes, the cross section of the wing changes continuously on other sections along the span. Figure 11 shows how the cross section at the middle of the second segment from the root deviates from the initial cross section (which is the S809 airfoil profile).

Table 1. Membrane properties, (u: upper, l: lower)

E	$84MPa$
ρ	$1400kg/m^3$
t	$0.48mm$
$\sigma^u_{chordwise}$	$180kPa$
$\sigma^u_{spanwise}$	$480kPa$
$\sigma^l_{chordwise}$	$180kPa$
$\sigma^l_{spanwise}$	$480kPa$

Table 2. Trailing edge cable properties

E	$125GPa$
ρ	$7800kg/m^3$
$radius$	$4mm$
σ	$30MPa$

Table 3. Rib properties

E	$190GPa$
ρ	$7800kg/m^3$
A	$2cm \times 12cm$

Wind Energ. Sci. Discuss., doi:10.5194/wes-2016-6, 2016
Manuscript under review for journal Wind Energ. Sci.
Published: 11 May 2016
© Author(s) 2016. CC-BY 3.0 License.

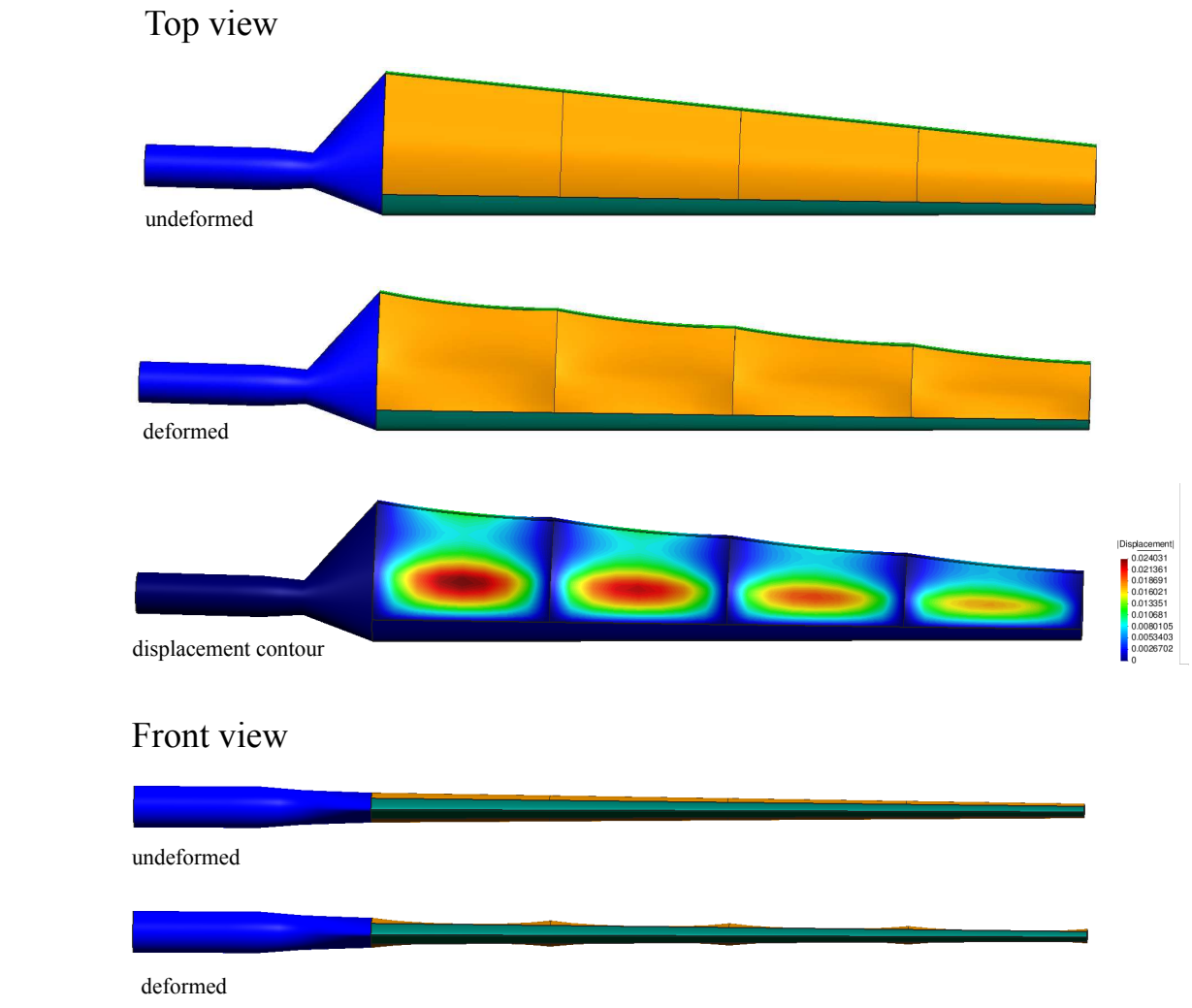

Figure 10. Form finding of the membrane blade. Undeformed and deformed geometry from top and front views.

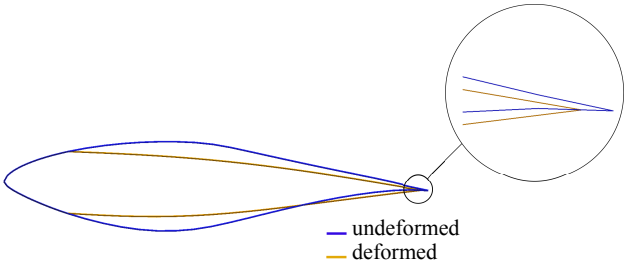

Figure 11. Form finding of the membrane blade (mid-span section, second segment from the root).

Wind Energ. Sci. Discuss., doi:10.5194/wes-2016-6, 2016
Manuscript under review for journal Wind Energ. Sci.
Published: 11 May 2016
© Author(s) 2016. CC-BY 3.0 License.



eawe european academy of wind energy
Open Access WIND ENERGY SCIENCE DISCUSSIONS

3.2 Fluid Setup

For the fluid side, SimpleFoam solver from OpenFOAM has been used for performing steady state CFD simulations. The schematic representation of the blocking strategy is presented in Figure 12. Computational domain together with the mesh in the vicinity of the blade is shown in Figure 13. The domain size is $15m \times 15m \times 45m$, which results in a blockage ratio of about 0.3%. The tip of the blade has a distance of $10m$ to the far field boundary. The domain is discretized with a total of 2.9 million cells (hexahedral and tetrahedral elements), which results in a maximum y^+ value of about 70.

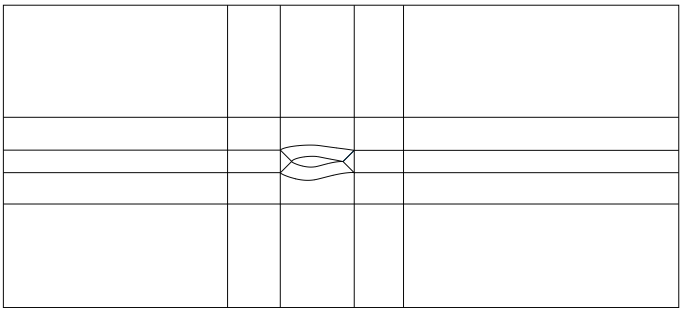

Figure 12. Blocking structure for the fluid mesh

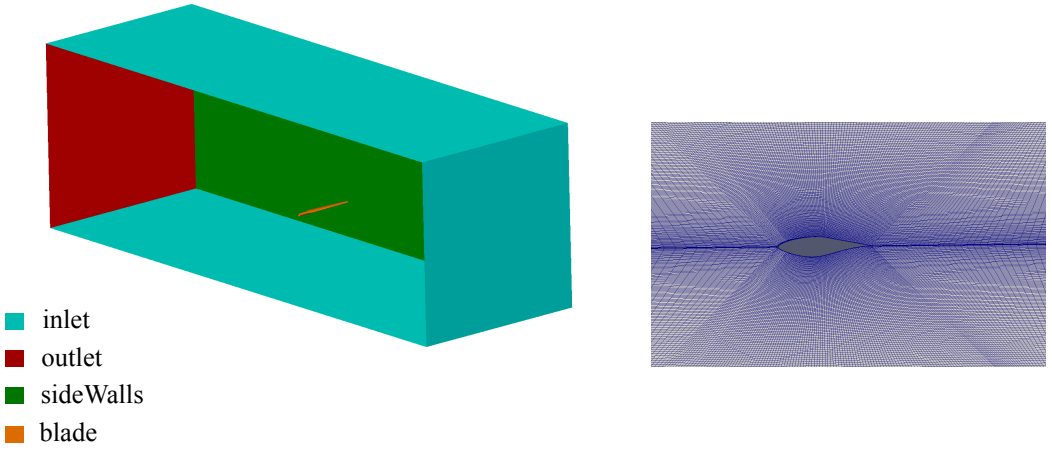

Figure 13. Left: Fluid Domain, Right: Fluid mesh in the vicinity of the blade

Wind Energ. Sci. Discuss., doi:10.5194/wes-2016-6, 2016
Manuscript under review for journal Wind Energ. Sci.
Published: 11 May 2016
© Author(s) 2016. CC-BY 3.0 License.



eawe european academy of wind energy
Open Access WIND ENERGY SCIENCE DISCUSSIONS

The $k-\omega SST$ model has been used. OpenFOAM wall functions are used at wing surface, kqRWallFunction for k and omegaWallFunction for ω. The velocity at the inlet is $30m/s$. The boundary conditions for fluid simulation are summarized in table 4.

Table 4. Boundary conditions for CFD simulations

boundary	U	p	k	ω
inlet	fixedValue uniform $(u_\infty, v_\infty, w_\infty)$	zeroGradient	fixedValue uniform $k = \frac{0.1U_\infty^2}{Re_L}$	fixedValue uniform $\omega = \frac{10*U_\infty}{L}$
outlet	zeroGradient	fixedValue uniform 0	zeroGradient	zeroGradient
sideWalls	symmetryPlane	symmetryPlane	symmetryPlane	symmetryPlane
blade	fixedValue uniform $(0,0,0)$	zeroGradient	kqRWallFunction uniform 1^{-10}	omegaWallFunction uniform $\omega = 10\frac{6\nu}{\beta_1(\Delta d_1)^2}$

3.3 FSI Simulations

FSI simulations were done for 6 different angles of attack from $0°$ to $9°$. In the following FSI_CFD us used for simulations using finite volume method on the fluid side and FSI_Panel is used for simulations which use panel method for flow modeling. Because of blade's deformation in FSI simulations, the fluid solver should in addition to solving the fluid flow problem, take care of the movement in the mesh as well. For FSI_CFD case the deformation of the blade, which as applied to the blade patch is diffused into the fluid domain. To solve the mesh motion problem the *displacementLaplacian* based solver from OpenFOAM is used with the *quadratic inverseDistance* diffusion method.

Convergence to steady state solution for the case of using panel method solver is about 30 times faster than using the simpleFoam solver from OpenFOAM as the fluid solver. The panel code was run on a single processor, while for OpenFOAM simulations 10 processors were used. For both cases a relaxation factor of 0.15 has been used for the displacement field for all angles of attack except for $\alpha = 7.5°$ and $\alpha = 9.0°$, where the relaxation factor was reduced to 0.1 to improve stability in FSI run. The relaxation factor (ω_r) is applied in order not to send the total calculated displacement at an increment to the fluid solver, but to send a fraction of that to improve stability of the coupling algorithm and preserve the quality of the mesh on the fluid side:

$$\mathbf{d}_{\Gamma_{I,sent}}^{n+1} = \omega_r \mathbf{d}_{\Gamma_{I,calculated}}^{n+1} + (1-\omega_r)\mathbf{d}_{\Gamma_I}^{n} \tag{26}$$

The relaxation factor should be kept below some limit (which is case dependent) for FSI_CFD simulations, otherwise the quality of the finite volume mesh cannot be preserved during the simulation and the simulation might crash as a result of having highly distorted elements in the mesh. The same relaxation factor is used for FSI_Panel case. The reason for using the same relaxation factor is to have a rather fair comparison between the convergence behavior of the two approaches, but it must

Wind Energ. Sci. Discuss., doi:10.5194/wes-2016-6, 2016
Manuscript under review for journal Wind Energ. Sci.
Published: 11 May 2016
© Author(s) 2016. CC-BY 3.0 License.



eawe european academy of wind energy
Open Access WIND ENERGY SCIENCE DISCUSSIONS

be mentioned, that for FSI_Panel cases a higher relaxation factor can be used as well to have faster convergence and yet not getting stability problems due to distorted element in the mesh, which is in this case just a discretized surface.

First, we compare the convergence behavior of the displacements to the steady state solution for each approach (Figure 14). Displacement of the point at the mid-span section of the second segment from the root with $x/c = 0.5$ is compared (c is the chord length). While with the panel method convergence is reached within 25 iterations, FSI simulation using SimpleFoam takes 450 iterations to converge. The time each iteration takes is also different in the two approaches. Overall, in case of the panel method convergence is reached approximately 30 times faster. For this particular case FSI_CFD simulation has taken about 10 hours to converge using 10 processors, but FSI_Panel has converged within about 20 minutes on a single processor. For $\alpha = 4°$ the converged displacement is $0.0221m$ from FSI_Panel and $0.0211m$ from FSI_CFD, which demonstrates clearly the applicability of the low-fidelity approach, provided that the blade operating condition is in agreement with the respective modeling assumptions (see section 2.1.2).

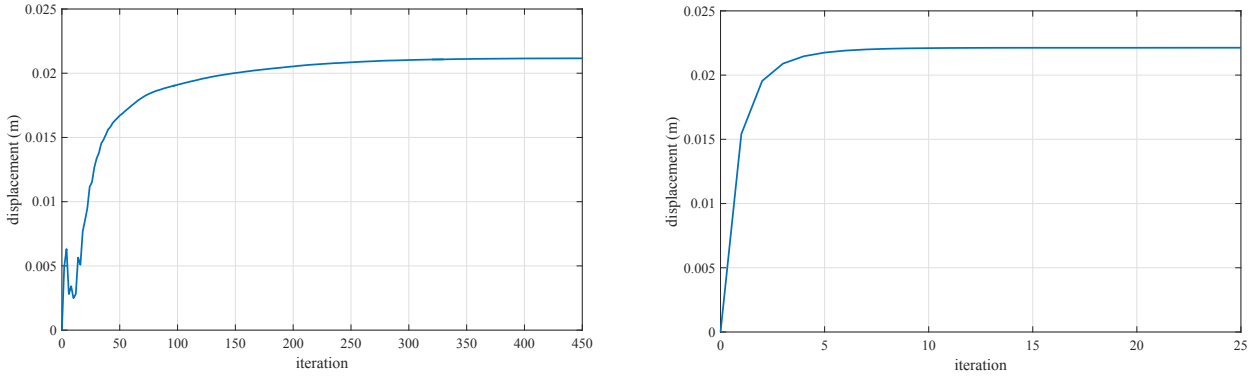

Figure 14. Convergence of the displacement for the selected monitor point. Left: FSI_CFD. Right: FSI_Panel.

The comparison of the two approaches for the selected monitor point is summarized in Table 5. For $\alpha = 0°$ the difference in the calculated displacement from the two approaches is 2.87%. The difference increases with angle of attack. For the base airfoil of the studied blade, the S809 profile, stall happens at $\alpha \approx 9°$. With the emergence of stall and flow separation, the assumptions of the panel method are no more valid. This explains the increased deviation of FSI_Panel result from FSI_CFD result for $\alpha = 9°$.

After local comparison of the calculated displacements for the two approaches in table 5 for a single monitor point, a more global comparison is made by comparing the converged cross section shape at the steady state. Figure 15 shows the cross section of the blade at the middle of the second segment from the root. For the upper surface of the blade there is a good agreement between the two methods, even though the difference increases with angle of attack which is to be expected. The difference in the converged shape is higher for the lower surface and specially for $\alpha = 7.5°$ and $\alpha = 9.0°$. It can be explained by the increased discontinuity in the slope of the surface at the point where the lower membrane is attached to the leading

Wind Energ. Sci. Discuss., doi:10.5194/wes-2016-6, 2016
Manuscript under review for journal Wind Energ. Sci.
Published: 11 May 2016
© Author(s) 2016. CC-BY 3.0 License.



eawe european academy of wind energy
Open Access WIND ENERGY SCIENCE DISCUSSIONS

Table 5. Comparison of displacement [m] in y direction for different angles of attack

$\alpha(deg)$	FSI_Panel	FSI_CFD	$\%diff$
0.0	0.0175	0.0170	2.87
2.0	0.0198	0.0189	4.74
4.0	0.0221	0.0211	4.73
6.0	0.0241	0.0231	4.38
7.5	0.0252	0.0241	4.53
9.0	0.0255	0.0237	7.68

edge mast. At the point of attachment exists a kink, which is much more visible for higher angles of attack. The local flow separation downstream of the kink is not captured by the panel method, which results in different pressure distributions and as a consequence different converged shapes for the two approaches.

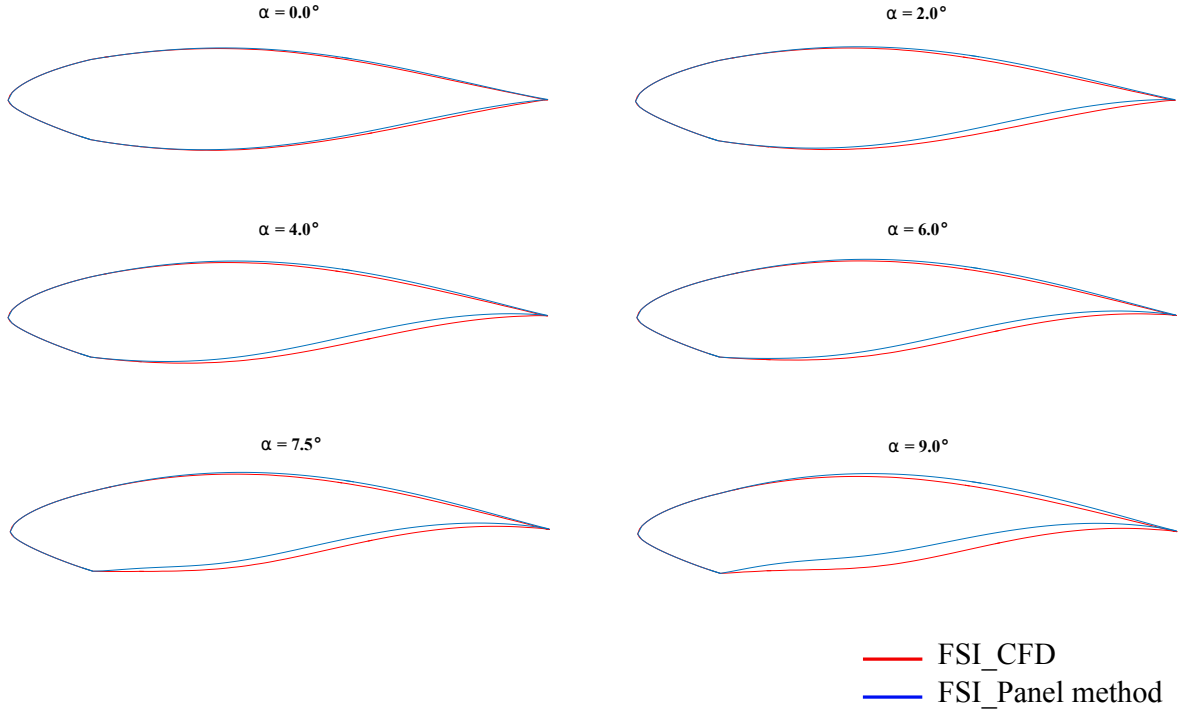

Figure 15. Comparison of the converged cross section at the mid-span section of the second segment from the root.

The concept of a membrane blade facilitates a lighter blade construction due to the optimal load carrying behavior and also due to its capability to alleviate peak loadings by deformation. Its flexibility is also an advantage in terms of dynamic (e.g. due to gusts) loading applied to the blade. It should also have an improved performance compared to rigid wing configurations in

Wind Energ. Sci. Discuss., doi:10.5194/wes-2016-6, 2016
Manuscript under review for journal Wind Energ. Sci.
Published: 11 May 2016
© Author(s) 2016. CC-BY 3.0 License.



eawe european academy of wind energy
Open Access WIND ENERGY SCIENCE DISCUSSIONS

stall region because of the so called "soft stall characteristics" of the membrane wings Maughmer (1979). In order to assess the aerodynamic performance of the studied blade, lift coefficient, drag coefficient and lift to drag ratio of the blade are compared with the rigid blade configuration (i.e. configuration before form finding). As it can be seen in Figure 16, for smaller angles of attack the membrane blade has smaller lift and drag coefficient compared with the rigid blade; however, with the increase of angle of attack higher lift and drag coefficients are observed for the membrane blade. Table 6 provides numeric comparison of the change in these coefficients compared with the rigid blade. The cross section of the membrane blade in the absence of aerodynamic load was shown in Figure 11 (the orange curve). The membrane blade has a pretty much symmetric profile in the unloaded state. For $\alpha = 0.0°$, the converged cross section is also a rather symmetric profile (Figure 15). This explains the big decrease in the lift coefficient of the membrane blade at $\alpha = 0.0°$, compared with the rigid blade with the asymmetric S809 airfoil. With the increase of angle of attack, the loading on the blade, and as a consequence the converged cross section profile, becomes more and more asymmetric which can be seen in Figure 15. Moreover the displacements in the membranes increase with the increase in angle of attack. It increases the thickness of the blade profile and as a consequence there is an improvement in the lift coefficient of the membrane blade compared with the rigid blade for higher angles of attack. The drag coefficient increases as well with the increase in angle of attack and the drag coefficient of the membrane blade is higher than that of the rigid blade. But the improvement in the lift coefficient is larger compared with the increase in the drag coefficient and consequently for $\alpha = 4.0°$ and higher angles of attack the lift to drag ratio for the membrane blade is higher compared with the conventional rigid blade. While having a higher lift coefficient and lift to drag ratio is not desired for stall controlled turbine like the NASA-Ames Phase VI rotor, it should be mentioned that the purpose of the current study is to investigate the characteristics of the membrane blade concept and make a comparison between the membrane blade and a conventional blade. No conclusion could be made at this stage, whether the concept should be utilized for pitch-controlled or stall-controlled turbines.

Table 6. Percentage change in aerodynamic characteristics of the membrane blade compared with the rigid blade

$\alpha(deg)$	0.0	2.0	4.0	6.0	7.5	9.0
Δc_L	-75.5427	-12.4708	7.4925	15.0273	17.6614	13.9290
Δc_D	-4.2353	-5.3452	-1.4706	3.4483	5.9390	2.9494
$\Delta(L/D)$	-74.4610	-7.5280	9.0968	11.1931	11.0652	10.6650

The cross section of the membrane blade varies along the span. Membrane deformation changes cross section properties of the wing like the maximum camber and thickness. The original S809 airfoil has a maximum camber of about 1% at 82.3% chord position, but for the membrane blade maximum camber and its location changes with angle of attack (table 7). It is also shown in Figure 17 that with the increase of angle of attack the maximum camber increases as well and in general the point of maximum camber moves slightly towards the leading edge of the wing.

The increase in lift coefficient for the membrane blade could also be seen in the pressure coefficient distribution over blade's surface. The pressure coefficient distribution over the middle span section of the second segment from the root is plotted in

Wind Energ. Sci. Discuss., doi:10.5194/wes-2016-6, 2016
Manuscript under review for journal Wind Energ. Sci.
Published: 11 May 2016
© Author(s) 2016. CC-BY 3.0 License.

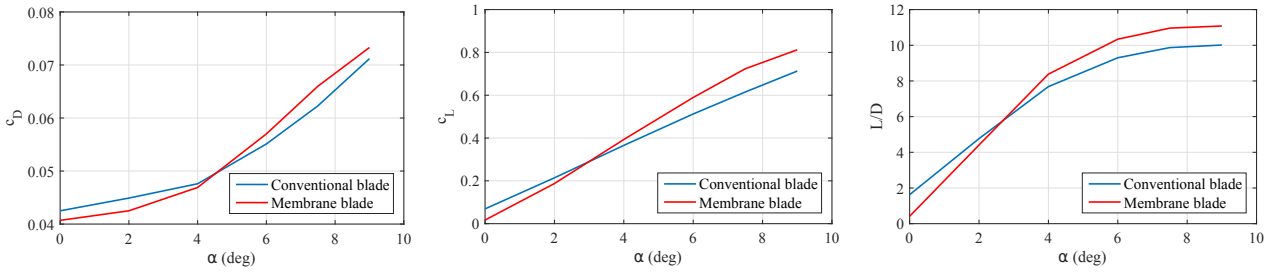

Figure 16. Comparison between the aerodynamic characteristics of the membrane blade and rigid blade

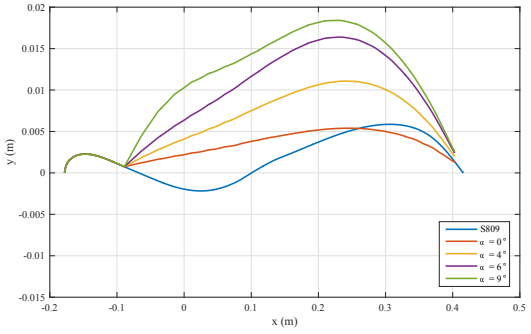

Figure 17. Comparison of the camber line at the middle span section of the second segment from the root.

Figure 18 and is compared with pressure coefficient distribution of the rigid blade for $\alpha = 6.0°$. The kink in the c_p distribution is due to slope discontinuity at the point where the lower membrane is attached to the rigid leading edge mast.

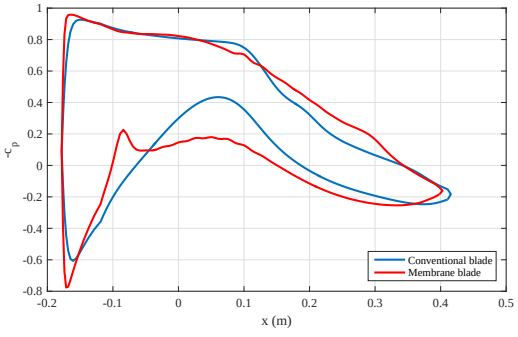

Figure 18. Pressure coefficient distribution over the middle span section of the second segment from the root.

Wind Energ. Sci. Discuss., doi:10.5194/wes-2016-6, 2016
Manuscript under review for journal Wind Energ. Sci.
Published: 11 May 2016
© Author(s) 2016. CC-BY 3.0 License.



eawe european academy of wind energy
Open Access WIND ENERGY SCIENCE DISCUSSIONS

Table 7. Maximum camber and its location for the middle span section of the second segment from the root

$\alpha(deg)$	0.0	2.0	4.0	6.0	7.5	9.0
Maximum Camber %	0.34	0.93	1.91	2.82	3.29	3.17
Location of maximum camber	71.48	73.53	73.51	71.45	69.40	69.40

4 Conclusion

Fluid-structure interaction simulation of a semi-flexible membrane blade configuration is done over a range of angles of attack. Two different fluid models were used: CFD simulation based on RANS equations and vortex panel method. The panel method saves computation time while providing a good accuracy up to an angle of attack of 6°. This makes the panel method an appropriate tool for early design stages of the membrane blade where an extensive parameter study needs to be done. Its accuracy could be improved by coupling boundary layer models with it. Comparing the performance of the membrane blade with its representative rigid counterpart the following main observations are made:

1. A higher lift curve slope for the membrane blade is observed. Even though at zero angle of attack the membrane blade has a smaller lift coefficient than the rigid blade, due to the higher slope of the lift curve, the membrane blade shows higher lift coefficient compared with the rigid blade.

2. With the increase of angle of attack the lift to drag ratio of the membrane blade becomes higher than that of the rigid blade.

3. The maximum camber and its location for a membrane blade depends on the angle of attack. The maximum camber of the membrane blade is higher than the rigid blade. With the increase of angle of attack there is a slight shift of the point of maximum camber toward the leading edge.

Acknowledgements. The provided support by the Deutsche Forschungsgemeinschaft (DFG) (BL 306/32-1) is gratefully acknowledged.

Wind Energ. Sci. Discuss., doi:10.5194/wes-2016-6, 2016
Manuscript under review for journal Wind Energ. Sci.
Published: 11 May 2016
© Author(s) 2016. CC-BY 3.0 License.



eawe european academy of wind energy
Open Access WIND ENERGY SCIENCE DISCUSSIONS

References

Abdulrahim M., Garcia H., Lind R.: Flight Characteristics of Shaping the Membrane Wing of a Micro Air Vehicle, AIAA J. of Aircraft, Vol. 42, No. 1, 131-137, doi: 10.2514/1.4782, 2005.

Barbarino S., Dettmer W., Friswell M.: Morphing Trailing Edges with Shape Memory Alloy Rods, ICAST 2010.

Barlas A.k., Tibaldi C., Zahle F., Madsen H.: Aeroelastic Optimization of a 10 MW Wind Turbine Blade with Active Trailing Edge Flaps, 34th Wind Energy Symposium, AIAA, doi: 10.2514/6.2016-1262, 2016.

Bletzinger K-U., Ramm E.: A General Finite Element Approach to the form Finding of Tensile Structures by the Updated Reference Strategy , International Journal of Space Structures, Vol. 14, 2, 131-145, 1999.

Blondeau J., Richeson J., and Pines J.D.: Desing, development and testing of a morphing aspect ratio wing using an inflatable telescopic spar, 44th AIAA/ASME/ASCE/AHS/ASC Structures, Structural Dynamics, and Materials Conference, doi:10.2514/6.2003-1718, 2003.

Bottasso C. L.,Croceb A, Gualdonib F, Montinarib P.: Load mitigation for wind turbines by a passive aeroelastic device, Journal of Wind Engineering and Industrial Aerodynamics, 148, 57-69, doi = 10.1016/j.jweia.2015.11.001, 2016.

Bowmann J., Sanders B., Cannon B., Kudva J, Joshi S., Weisshaar T.: Development of Next Generation Morphing Aircraft Structures, 48th AIAA/ASME/ASCE/AHS/ASC Structures, Structural Dynamics, and Materials Conference, Honolulu, Hawaii, doi:10.2514/6.2007-1730, April 2007.

Fink M.: Full-scale Investigation of the Aerodynamic Characteristics of a Model Employing a Sailwing Concept, NASA-TN-D-4062, 1967.

Fink M.: Full-scale Investigation of the Aerodynamic Characteristics of a Sailwing of Aspect Ratio 5.9, NASA-TN-D-5047, 1969.

Hand M., Simms D., Fingersh L., Jager D., Cotrell J., Schreck S., Larwood S.: Unsteady aerodynamics experiment phase VI: wind tunnel test configurations and available data campaigns, Technical Report NREL/TP-500-29955, NREL, Golden, CO, USA, 2001.

Katz J, Plotkin A: Low Speed Aerodynamics, Cambridge, Cambridge Univ. Press, 2008.

Kupzok A. M.: Modeling the Interaction of Wind and Membrane Structures by Numerical Simulation, Technical University of Munich, 2009.

Levin O., Shyy W.: Optimization of a flexible low Reynolds number airfoil, 39th Aerospace Sciences Meeting and Exhibit, Aerospace Sciences Meetings, doi:10.2514/6.2001-125, 2001.

Lian Y., Shyy W.: Numerical Simulation of Membrane Wing Aerodynamics for Micro Air Vehicle Applications, AIAA J. of Aircraft, Vol. 42, No. 4, 865-873, doi: 10.2514/1.5909, 2005.

Maughmer M.D.: A Comparison of the Aerodynamic Characteristics of Eight Sailwing Airfoil Sections, Proceedings of the 3rd International Symposium on the Science and Technology of Low Speed and Motorless Flight, Hampton, VA, USA, 155-176, 1979.

Maughmer M.D.: Optimization and Characteristics of a Sailwing Windmill Rotor, Princeton University, 1976.

Menter F.R.: Two-Equation Eddy-Viscosity Turbulence Models for Engineering Applications, AIAA Journal, vol. 32, No. 8, 1598-1605, doi: 10.2514/3.12149, 1994.

Ormiston R.: Theoretical and Experimental Aerodynamics of the Sailwing, J. of Aircraft, Vol. 8, No. 2, pp. 77-84, doi: 10.2514/3.44232, 1971.

Otto F., Rasch B.: Finding Form, Deutscher Werkbund Bayern, Edition A, Menges, 1995.

Patankar S.V., Spalding D.B.: A calculation procedure for heat, mass and momentum transfer in three-dimensional parabolic flows, International Journal of Heat and Mass Transfer, Vol. 15, Issue 10, 1787-1806, doi: 10.1016/0017-9310(72)90054-3, 1972

Saeedi M., Wüchner R., Bletzinger K.-U.: Multi-fidelity Fluid-Structure Interaction Analysis of a Membrane Wing, 17th International Conference on Applied Aerodynamics and Aeromechanics, London, 2015.

Wind Energ. Sci. Discuss., doi:10.5194/wes-2016-6, 2016
Manuscript under review for journal Wind Energ. Sci.
Published: 11 May 2016
© Author(s) 2016. CC-BY 3.0 License.



Schek H-J.: The force density method for form finding and computations of general networks, Computer Methods in Applied Mechanics and Engineering,Vol. 3, No. 1, 115-134, doi: 10.1016/0045-7825(74)90045-0, 1974.

Valasek J.: Morphing Aerospace Vehicles and Structures. John Wiley, 2012.

Wakefield D.S.: Engineering analysis of tension structures: theory and practice, Engineering Structures, Vol. 21, No. 8, 680-690, doi: 10.1016/S0141-0296(98)00023-6, 1999.

Wang T., Wüchner R., Sicklinger S., Bletzinger K.-U.: Assessment and improvement of mapping algorithms for non-matching meshes and geometries in computational FSI, J. Computational Mechanics, doi=10.1007/s00466-016-1262-6, 2016.

Waszak R.M., Jenkins N.L., Ifju P.: Stability and Control Properties of an Aeroelastic Fixed Wing Micro Aerial Vehicle, AIAA Atmospheric Flight Mechanics Conference and Exhibit, Guidance, Navigation, and Control and Co-located Conferences, Montreal, Canada, doi:10.2514/6.2001-4005, 2001.

Wüchner R., Bletzinger K.-U.: Stress-adapted numerical form finding of pre-stressed surfaces by the updated reference strategy, International Journal for Numerical Methods in Engineering, Vol. 64, No. 2, 143-166, doi: 10.1002/nme.1344, 2005.

Wüchner R., Kupzok A., Bletzinger K.-U.: A framework for stabilized partitioned analysis of thin membrane-wind interaction, International Journal of Numerical Methods in Fluids, Vol. 54, No. 6-8, 945-963, doi:10.1002/fld.1474, 2007.